

PAPER

miRNA induced co-differentiation and cross-talk of adipose tissue-derived progenitor cells for 3D heterotypic pre-vascularized bone formation

To cite this article: Nazmiye Celik et al 2021 Biofabrication 13 044107

View the article online for updates and enhancements.

You may also like

- MicroRNA-mediated regulatory circuits: outlook and perspectives
 Davide Cora', Angela Re, Michele Caselle et al.
- Fabrication of vascularized tissue constructs under chemically defined culture conditions Gopu Sriram, Harish K Handral, Shu Uin Gan et al.
- Endothelial cells support osteogenesis in an in vitro vascularized bone model developed by 3D bioprinting Irene Chiesa, Carmelo De Maria, Anna Lapomarda et al.



Breath Biopsy® OMNI

The most advanced, complete solution for global breath biomarker analysis





Expert Study Design & Management



Robust Breath Collection



Reliable Sample Processing & Analysis



In-depth Data Analysis



Interpretation

Biofabrication



RECEIVED 14 March 2021

14 Maich 20

REVISED 31 August 2021

ACCEPTED FOR PUBLICATION
3 September 2021

PUBLISHED

17 September 2021

PAPER

miRNA induced co-differentiation and cross-talk of adipose tissue-derived progenitor cells for 3D heterotypic pre-vascularized bone formation

Nazmiye Celik^{1,2}, Myoung Hwan Kim^{2,3}, Daniel J Hayes^{2,3,4,*} and Ibrahim T Ozbolat^{1,2,3,4,5,*} ©

- Department of Engineering Science and Mechanics, Pennsylvania State University, 212 Earth-Engineering Sciences Bldg., University Park, PA 16802, United States of America
- ² The Huck Institutes of the Life Sciences, Penn State University, University Park, PA 16802, United States of America
- Department of Biomedical Engineering, Pennsylvania State University, Chemical and Biomedical Engineering Bldg., University Park, PA 16802, United States of America
- ⁴ Materials Research Institute, Penn State University, University Park, PA 16802, United States of America
- Department of Neurosurgery, Penn State College of Medicine, Hershey, PA 17033, United States of America
- * Authors to whom any correspondence should be addressed.

E-mail: djh195@psu.edu and ito1@psu.edu

Keywords: miRNA, stem cells, pre-vascularization, bone, spheroid assembly, bioprinting

Supplementary material for this article is available online

Abstract

Engineered bone grafts require a vascular network to supply cells with oxygen, nutrients and remove waste. Using heterotypic mature cells to create these grafts in vivo has resulted in limited cell density, ectopic tissue formation and disorganized tissue. Despite evidence that progenitor cell aggregates, such as progenitor spheroids, are a potential candidate for fabrication of native-like pre-vascularized bone tissue, the factors dictating progenitor co-differentiation to create heterotypic pre-vascularized bone tissue remains poorly understood. In this study, we examined a three-dimensional heterotypic pre-vascularized bone tissue model, using osteogenic and endotheliogenic progenitor spheroids induced by miR-148b and miR-210 mimic transfection, respectively. Spheroids made of transfected cells were assembled into heterotypic structures to determine the impact on co-differentiation as a function of micro-RNA (miRNA) mimic treatment group and induction time. Our results demonstrated that miRNAs supported the differentiation in heterotypic structures, and that developing heterotypic structures is determined in part by progenitor maturity, as confirmed by gene and protein markers of osteogenic and endotheliogenic differentiation and the mineralization assay. As a proof of concept, miRNA-transfected spheroids were also bioprinted using aspiration-assisted bioprinting and organized into hollow structures to mimic the Haversian canal. Overall, the presented approach could be useful in fabrication of vascularized bone tissue using spheroids as building blocks.

1. Introduction

Skeletal defects resulting from trauma, pathological degeneration or tumor resection is a vital issue for orthopedic surgery [1]. Bone grafts (including allografts and autografts) are a standard technique to address bone defects, but these grafts frequently fail due to lack of tissue vascularization, integration with the circulatory system and active perfusion during bone repair [2]. As such, vascularization remains one of the unmet clinical needs to ensure the success of engineered bone in clinics. Attempts to improve

bone graft vascularization using mature donor osteoblasts and endothelial cells often yields reduced tissue volume with deficient tissue integration and can lead to robust host response, while the use of diffusible cytokines *in vivo* has resulted in ectopic tissue formation and disorganized tissue [3–6]. Implantation of early-stage progenitor cells can improve tissue integration and reduce the host immune response [6], potentially providing a means to improved vascularized bone grafts but the factors dictating progenitor co-differentiation to create complex heterotypic vascularized bone tissue remains poorly understood.

Progenitor cell aggregates and engineered implants are potential candidate in bone tissue regeneration [2]. Adipose-derived stem cells (ADSCs), a type of mesenchymal stem cell (MSC) isolated from adipose tissue, have received substantial attention as a cell type for bone regeneration as they are clinically accessible [7] and available in large numbers, and possess multipotent differentiation making them an ideal cell source for orthopedic regeneration [8]. Interest in gene therapy for controlled differentiation has increased substantially in recent years [9, 10]. In particular, the use of microRNAs (miRNAs) has been an important development in modulation of the function and differentiation of stem/progenitor cells [11]. miRNAs are small non-coding RNAs that can regulate gene expression at the post-transcriptional level by binding to complementary sites on target messenger RNAs [11]. Studies have demonstrated that miR-148b could induce osteogenesis in bone marrow-derived stem cells and ADSCs de novo with a single transfection [6, 12–14]. Additionally, it has been demonstrated that miR-210, often described as the master hypoximiR (hypoxia-inducible miR), can induce endothelial differentiation in certain stem cells populations [15].

Although classic scaffold-based approaches have demonstrated feasibility for tissue regeneration [16, 17], these approaches still have many pitfalls [17, 18], such as scaffold degradation, limited cell density, and non-acceptable extracellular matrix (ECM) rigidity [19] for the stem cell differentiation purpose. Alternatively, three-dimensional (3D) spheroids, as a scaffold-free approach, relies on only cells and their secreted ECM components. This process enables the creation of high-fidelity tissue models that are able to mimic natural tissue microenvironment in terms of cell-cell and cell-ECM interactions, and to better explore the phenomenon of cellular cross-talk during tissue formation [20]. ADSC spheroids have recently been explored as a promising approach in bone tissue regeneration due to their capacity for higher cell densities and suitability for graft fabrication [20]. Overall, using spheroids as building blocks for scaffold-free strategies can increase cell density and facilitate the essential environment for progenitor cell differentiation for biofabrication purposes [17].

In this work, we examined the impact of endotheliogenic and osteogenic co-differentiation on the development of heterotypic spheroid structures as a step toward making spheroidal building blocks for pre-vascularized bone formation. Osteogenic and endotheliogenic progenitor spheroids were induced by miRNA mimic transfection and assembled into heterotypic structures to determine the impact on co-differentiation, as a function of miRNA mimic treatment group and induction time. Gene and protein

markers of osteogenic and endotheliogenic differentiation were assessed, and mineralization and spheroid fusion during heterotypic culture was evaluated. Finally, miR-148b and -210 transfected spheroids were bioprinted and organized into hollow structures to mimic the Haversian canal showing the scalable fabrication of tissues as a proof of concept.

2. Materials and methods

2.1. Isolation and culture of human ADSCs

To obtain Human ADSCs, surgically discarded adipose tissues were obtained from patients who underwent an elective adipose tissue removal process at the Pennsylvania State University (Hershey, PA) with patient's consent and approval from the Institutional Review Board (IRB protocol # 00004972). Human ADSCs were isolated using the protocol as we previously described [21, 22]. The sorted Human ADSCs were cultured in 50:50 mixture of Dulbecco's modified Eagle medium and Ham's nutrient mixture F-12 (DMEM/F12) (Corning, Manassas, VA) supplemented with 20% fetal bovine serum (FBS) (R&D Systems, Minneapolis, MN), 100 U ml⁻¹ penicillin and 100 $\mu\mathrm{g}~\mathrm{ml}^{-1}$ streptomycin (Corning, Manassas, VA) at 37 °C with 5% CO₂. Cell medium was changed every other day.

2.2. Osteogenic and endotheliogenic differentiation with chemical transfection via miRNAs

DMEM/F12, lipofectamine RNAiMAX transfection reagent, and Opti-MEM reduced serum medium were purchased from ThermoFisher Scientific (Waltham, MA), custom oligonucleotides (miR-210: 5'-CUG UGC GUG UGA CAG CGG CUG A-3'; miR-148b: 5' UCA GUG CAU CAC AGA ACU UUG U 3') were ordered from Integrated DNA Technologies (Coralville, IA).

Cells were seeded at a density of 1×10^6 in 75 cm² cell culture flasks. ADSCs were transfected with miR-148b and miR-210 mimic separately when cells reached a confluence of 80% before being seeded in opti-MEM medium (Gibco, Carlsbad, CA) for 24 h. Invitrogen Lipofectamine RNAiMAX transfection reagent (Thermo Fisher Scientific, Waltham, MA) was used for the transfection and was mixed with miR-148b or miR-210 according to the manufacturer's protocol. Transfection occurred over 24 h. The final concentration of miR-148b and miR-210 in opti-MEM medium was determined to be 200 nM for a total volume of 10 ml solution. The 10 ml solution was then transferred to a 75 cm² cell culture flask and incubated at 37 °C and 5% CO2 for 24 h. Transfected cells were collected by trypsinization for use in spheroid formation.

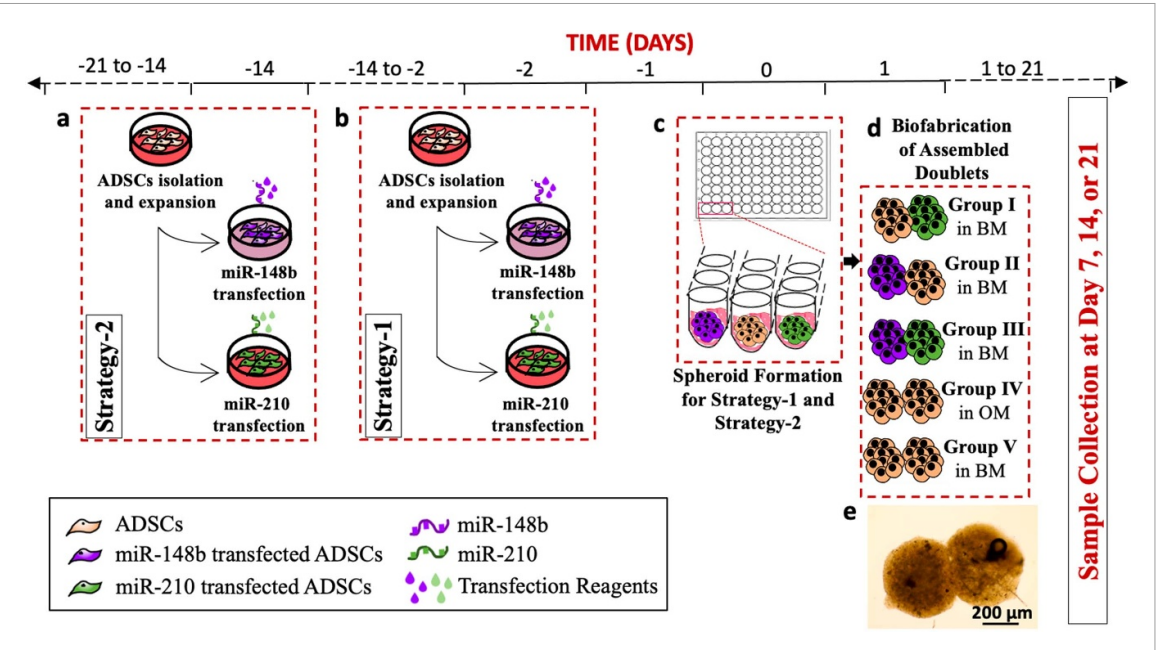


Figure 1. A schematic diagram describing biofabrication of doublet structures using miR-210 and miR-148b transfected spheroids. (Note: BM stands for basal medium and OM stands for osteogenic medium.)

2.3. Fabrication of 3D spheroids

To fabricate spheroids, human ADSCs were harvested with trypsin and collected by centrifugation at 1600 $\times g$ for 4 min. ADSCs were reconstituted to 2.5×10^5 cells ml⁻¹. The cell suspension (200 μ l) was pipetted into each well of a U-bottom 96-well plate (Greiner Bio-One, Monroe, NC). The 96-well plate was then incubated in a humidified atmosphere with 5% CO₂ at 37 °C overnight for spheroid formation. Spheroids were cultured with basal medium, and the medium was changed every other day. For a positive control group, spheroids were differentiated in osteogenic medium, which was changed every other day. After 21 d of differentiation, fabricated spheroids were harvested by firmly pipetting growth media up and down to dislodge spheroids from the 96-well plate.

2.4. Osteogenic differentiation using induction medium

The basal medium, DMEM F-12, was supplemented with 10% FBS and 1% antibiotic solution (10 000 μ g ml⁻¹ with penicillin and streptomycin). For osteogenic differentiation, the basal media was supplemented with dexamethasone (0.1 μ M), ascorbate-2-phosphate (50 μ M), and β -glycerophosphate (10 mM), and spheroids were cultured at 37 °C and 5% CO₂. Osteogenic medium was changed every 3 d.

2.5. Fabrication of doublet structures

To evaluate the early- and late-stage transfection effect on osteogenic and endotheliogenic formation, two different strategies were followed. In Strategy-1, ADSCs were cultured in monolayer for 2 d after the chemical transfection, followed by fabrication and culture of spheroids for 21 d in basal medium. In Strategy-2, ADSCs were cultured in monolayer for 14 d, followed by fabrication and culture of spheroids for 21 d in basal medium. For all groups, the total differentiation period in the form of spheroids was maintained at 21 d.

For each strategy, five different groups were assigned to understand the differentiation phenomena in different combinations of spheroids. In Group I, a spheroid formed by non-transfected ADSCs, and a spheroid formed by miR-210 transfected ADSCs were assembled manually and cultured for 21 d in basal medium. In Group II, a spheroid formed by miR-148b transfected ADSCs and a spheroid formed by non-transfected ADSCs were assembled manually and cultured for 21 d in basal medium. In Group III, a spheroid formed by miR-148 transfected ADSCs and a spheroid formed by miR-210 transfected ADSCs were assembled manually and cultured for 21 d in basal medium. In Group IV (positive control group), two spheroids formed by non-transfected ADSCs were assembled manually and cultured for 21 d in osteogenic medium. In Group V (negative control group), two spheroids formed by nontransfected ADSCs were assembled manually and cultured for 21 d in basal medium. Manual assembly was performed by picking spheroids and placing them next to each other onto a glass bottom 35 mm cell culture plate (Greiner Bio-One, Monroe, NC). The reader is referred to figure 1 for a systematic illustration of different strategies and groups utilized in this study.

Table 1. Primers of the measured mRNA for qRT-PCR.

Gene	Forward primer	Reverse primer
OSTERIX	CCT CTG CGG GAC TCA ACA AC	AGC CCA TTA GTG CTT GTA AAG G
COL1	ATG ACT ATG AGT ATG GGG AAG CA	TGG GTC CCT CTG TTA CAC TTT
BSP	AAC GAA GAA AGC GAA GCA GAA	TCT GCC TCT GTG CTG TTG GT
RUNX2	GGT TAA TCT CCG CAG GTC ACT	CAC TGT GCT GAA GAG GCT GTT
ANGPT1	GTT CAG TCA GGG GAG CAG AG	CTC CAG ACC CAC CAC AAG AT
PECAM1	TAA TAC AAC ATC CAC GAG GGT CC	ACA AAA TTG CTT GCT AAA GAA GTG G
GAPDH	ATG GGG AAG GTG AAG GTC G	GGG GTC ATT GAT GGC AAC AAT A

2.6. Gene expression of doublet structures using quantitative real-time polymerase chain reaction (qRT-PCR)

To evaluate the osteogenic and endotheliogenic gene expression profiles using qRT-PCR, five different groups for both strategies were harvested at Days 7, 14 and 21, and samples were homogenized in TRIzol reagent (Life Technologies, CA), followed by adding 0.2 ml chloroform per 1 ml TRIzol reagent and centrifuging the mixture at 12 000 $\times g$ for 15 min at 4 °C. The upper aqueous phase with RNA was transferred and the RNA was then precipitated by adding 0.5 ml isopropyl alcohol per 1 ml TRIzol reagent, followed by centrifuging at 12 000 $\times g$ for 10 min at 4 °C. Subsequently, the precipitated RNA was rinsed twice with 75% ethanol, air-dried for 10 min and then dissolved in 50 μ l diethyl pyrocarbonate-treated water. RNA concentration was measured using a Nanodrop (Thermo Fisher Scientific, PA). Reverse transcription was performed using AccuPower® CycleScript RT PreMix (BIONEER, Korea) following the manufacturer's instructions. Gene expression was analyzed quantitatively with SYBR Green (Thermo Fisher Scientific, PA) using a QuantStudio 3 PCR system (Thermo Fisher Scientific). Osteogenic and endotheliogenic genes tested included OSTERIX (transcription factor Sp7), COL-1 (collagen type-1), RUNX2 (runtrelated transcription factor 2), BSP (bone sialoprotein), PECAM-1 (platelet/endothelial cell adhesion molecule-1), and ANGPT-1 (angiopoietin-1). The reader is referred to table 1 for the gene sequences. Expression levels for each gene were normalized to glyceraldehyde 3-phosphate dehydrogenase (GAPDH). The fold change of Group V (negative control) at Days 7, 14, and 21 were set as one-fold and values in all groups were normalized with respect to that of Group V.

2.7. Mineralization staining

Hydroxyapatite deposition of doublet structures for each group and strategy was assessed after 7, 14, and 21 d of culture by Osteoimage™ mineralization staining. Spheroids were rinsed with Dulbecco's phosphate buffered saline (DPBS) and fixed in 10% neutral buffered formalin for 3 h at room temperature (25 °C). Samples were gradually dehydrated in alcohol and embedded in paraffin using a Leica TP 1020 automatic tissue processor (Leica,

Buffalo Grove, IL). Then, samples were sectioned in 10 mm thickness with a Shandon Finesse® Paraffin microtome (Thermo Electron Corporation, Waltham, MA). Osteoimage™ Mineralization Assay (Lonza) was performed to assess mineralization. Sectioned samples were washed three times with Osteoimage[™] wash buffer at room temperature then incubated with 2 ml of staining reagent for 30 min in dark at room temperature. The samples were then imaged using Zeiss LSM 880 Airyscan confocal microscope (Zeiss, Oberkochen, Germany). Collected images were used to determine Osteoimage™ fluorescence intensities and characterized using Image J (National Institutes of Health, Bethesda, MD). Images were converted to RGB color and then the mean gray value of the green channel was determined from the histogram plots.

2.8. Immunohistochemistry (IHC) study

Sectioned samples were permeabilized in 0.2% Triton X-100 for 30 min and blocked with 2.5% normal goat serum (NGS) for 60 min at room temperature. To visualize osteogenic and endotheliogenic tissue formation, samples were incubated with mouse anti-RUNX2 primary antibody (1:500 in 2.5% NGS; Cat. No: ab76956; Abcam, Cambridge, UK) and rabbit anti-VE Cadherin (1:500 in 2.5% NGS; Cat. No: ab33168, Abcam, Cambridge, UK) for overnight, washed three times with DPBS, and incubated with goat anti-mouse Alexa Fluor 488 secondary antibody (1:200 in 2.5% NGS; Cat. No: ab150113; Abcam, Cambridge, UK), goat anti-rabbit Alexa Fluor 647 secondary antibody (1:200 in 2.5% NGS; Cat. No: ab150079; Abcam, Cambridge, UK) and 40,6-diamidino-2-phenylindole (DAPI; 1:200 in 2.5% NGS) for 3 h. Stained samples were then washed three times with DPBS and imaged using a Zeiss LSM 880 Airyscan confocal microscope (Zeiss, Oberkochen, Germany) using a Plan-Apochromat 10×/0.30 M27 objective via ZEN 2.3 SP1 software. All groups for both strategies were taken at 2048×2048 pixels at $1 \times$ zoom exciting Alexa Fluor® 405, 488 and 568 nm wavelengths at 4.5, 2% and 4% laser power for DAPI, RUNX2 and VE Cadherin, respectively.

RUNX2 and VE Cadherin fluorescence intensities were determined from IHC images and characterized using Image J. Images were converted to RGB color.

The mean gray value for the green and red channels was determined from histogram plots in order to reveal RUNX2 and VE Cadherin intensities for each group and strategy, respectively.

2.9. Hematoxylin and eosin (H&E) staining

To confirm morphologies of doublet structures, sectioned samples were also stained with H&E. Doublet structures for all groups for both strategies were fixed after 7, 14, and 21 d of culture in 10% neutral buffered formalin overnight and gradually dehydrated in alcohol. Samples were then embedded in paraffin blocks using the Leica TP 1020 automatic tissue processor and cut into 10 μ m sections with the Shandon Finesse® Paraffin microtome. After collecting the sections on glass microscope slides, samples were placed in a Leica Autostainer XL (Leica, Germany) based on the manufacturer's protocol. After the staining process, stained sections were mounted using a xylene substitute mountant (Thermo Scientific, Waltham, MA) and kept at room temperature to dry overnight. Stained samples were imaged using an EVOS microscope (Invitrogen, MA).

2.10. Fusion of doublets

Optical images of three doublets for each group and strategies imaged using the EVOS microscope after 7, 14, and 21 d of culture. Doublet length and width, contact length, and intersphere angle were measured by Image J [23].

2.11. Preparation of alginate (Alg) microgels

Sodium Alg (Sigma Aldrich Inc., MO, USA) was dissolved in ultra-purified water at a concentration of 0.5% w/v to prepare Alg microgel crosslinked with 4% calcium chloride (CaCl₂, Sigma Aldrich Inc., MO, USA) by adding dropwisely, following our previous studies [24, 25]. After crosslinking of Alg for 30 min, crosslinked Alg particles were collected, washed thrice with ultra-purified water to remove CaCl₂ solution and uncrosslinked Alg residues. The Alg particles were blended at 465 $\times g$ for 30 min to obtain Alg microgels using a commercial blender. The resultant microgels were then divided into 50 ml conical tubes and centrifuged at 2000 $\times g$ for 5 min. All equipment used for the preparation of Alg microgels were sterilized with 70% ethanol and ultraviolet light for 30 min.

2.12. Bioprinting of a Haversian canal model

A custom-made aspiration-assisted bioprinting system, reported in our previous studies [24–26], was utilized to develop a model of the Haversian canal. For fabrication of the Haversian canal, bioprinting parameters, such as bioprinting speed and aspiration pressure, optimized in [24] were utilized.

First, to demonstrate the organization of spheroids in bioprinted structures and show the positioning of osteogenic and endotheliogenic spheroids, ADSCs were stained with 5 μ M of CellTrackerTM Green CMFDA dye (Cat. No: C7025; Invitrogen, Carlsbad, CA, USA) and CellTracker™ red CMTPX dye (Cat. No: C34552; Invitrogen, Carlsbad, CA, USA) according to the manufacturer's instructions, respectively. Labeled ADSCs were incubated in opti-MEM medium (Gibco, Carlsbad, CA) containing dye solution for 45 min. After replacement with fresh basal medium and incubation in a humidified atmosphere with 5% CO₂ at 37 °C overnight, labeled cells were collected with trypsin. Collected ADSCs were used to prepare spheroids labelled with CellTracker™ Green CMFDA or CellTracker™ red CMTPX. Labeled ADSC spheroids were bioprinted to form hollow structures (inner: CMTPX-labeled spheroids; outer: CMFDA-labeled spheroids), which were monitored using an EVOS FL cell imaging system (Thermo Fisher Scientific, Waltham, MA).

Second, to demonstrate the Haversian canal model, Group III spheroids (miR-148b transfected ADSC spheroids and miRNA-210 transfected ADSC spheroids) were fabricated by following Strategy-2. ADSC spheroids were then bioprinted to form hollow structures (inner: ADSC spheroids transfected with miR-210; outer: ADSC spheroids transfected with miR-148b) (see supplementary video 1 available online at stacks.iop.org/BF/13/044107/mmedia). After bioprinting, structures were maintained in Alg microgels for 5 d until the fusion of spheroids was realized and then the structures were removed using 4 w/v% sodium citrate (Sigma Aldrich Inc.) as explained before [24, 25]. Bioprinted structures were washed with DPBS (Corning, NY, USA) and cultured with basal medium, DMEM F-12, was supplemented with 10% FBS and 1% antibiotic solution (10 000 μ g ml⁻¹ with penicillin and streptomycin). The bioprinted structures were harvested on Day 14 and fixed in 4% paraformaldehyde in DPBS for immunostaining analysis as explained in section 2.8.

2.13. Statistical analysis

All values were presented as mean \pm standard deviation. Multiple comparisons were analyzed using one-way analysis of variance (ANOVA) followed by Post hoc Tukey's multiple-comparison test to determine the individual differences among the groups. Differences were considered significant at $p^* < 0.05$, $p^{**} < 0.01$, $p^{***} < 0.001$, and $p^{****} < 0.0001$. All statistical analysis was performed by Prism Software (GraphPad Software Inc., La Jolla, CA).

3. Results

In order to determine the optimal time period to obtain an effective miRNA transfection, two different strategies were evaluated: Strategy-1, in which transfected ADSCs were cultured for 2 d in two dimensions (2D) post transfection prior to spheroid formation,

and Strategy-2, in which transfected ADSCs were cultured for 14 d in 2D post transfection prior to spheroid formation.

To investigate the effect of different spheroid combinations on co-differentiation, five different groups were designed as depicted in figure 1 and their differentiation potential was evaluated in detail to determine the most appropriate combination enabling pre-vascularized bone formation from complex heterotypic aggregates. In Group I, a spheroid formed using non-transfected ADSCs and a spheroid formed using miR-210 transfected ADSCs were assembled and cultured in basal medium for 21 d. In Group II, a spheroid formed using non-transfected ADSCs and a spheroid formed using miR-148 transfected ADSCs were assembled and cultured in basal medium for 21 d. In Group III, a spheroid fabricated using miR-148b transfected ADSCs and a spheroid fabricated using miRNA-210 transfected ADSCs were assembled and cultured in basal medium for 21 d. In Group IV, two spheroids formed using nontransfected ADSCs were assembled and cultured in osteogenic medium for 21 d as the positive control group. In Group V, two spheroids fabricated using non-transfected ADSCs were assembled and then cultured in basal medium for 21 d as the negative control group.

The relative osteogenic gene expression of the doublet structures was measured by qRT-PCR on Days 7, 14, and 21. For both strategies, the expression of osteogenic genes including RUNX2 (runtrelated transcription factor 2) (figure 2(a)), Col-1 (figures 2(b) and (c)) OSTERIX (transcription factor Sp7) (figure 2(c)), and BSP (figure 2(d)) were determined. Although Strategy-1 showed earlier onset in gene expression of osteogenic markers for Groups II and III as compared to Strategy-2 at Day 7 and 14, all osteogenic genes of groups prepared using transfected cells (Groups II and III) showed a greater level of expression using Strategy-2 as compared to Strategy-1 at Day 21. In Strategy-1, Group II exhibited significantly increased expression levels for osteogenic genes (BSP: \sim 117-folds and OSTERIX: \sim 602-folds at Day 21) with values that were similar to the positive control group (BSP: \sim 28-folds and OSTERIX: ~85-folds). RUNX2 gene expression level significantly decreased for all groups by Day 21 in Strategy-1. Group I, which was formed with miR-210 transfected cells and non-transfected ADSCs, did not display any meaningful upregulation of osteogenic markers for both Strategy-1 and -2 at Day 21. Expression of RUNX2 (\sim 21-folds), BSP (\sim 406-folds), and OSTERIX (~3-folds) for Group III in Strategy-2 on Day 21 was significantly higher than those in Strategy-1. Our results indicate that assembling a miR-148b transfected spheroid with a miR-210 transfected spheroid (Group III) supported higher level osteogenic marker expressions compared to the use of a single miRNA mimic or osteogenic medium.

The relative endotheliogenic gene expression of doublet structures was measured by qRT-PCR on Days 7, 14, and 21. The expression of endotheliogenic genes, including ANGPT-1 (figure 3(b)) and PECAM-1 (figure 3(a)), were determined. Overall, endotheliogenic gene expression of groups prepared with miRNA transfected cells (Group I and Group III) was greater in Strategy-2 as compared to Strategy-1. In Strategy-1, Group II exhibited significantly increased expression levels for PECAM-1 and ANGPT-1 at Days 14 and 21. The expression levels of endotheliogenic genes in Group II peaked at Day 14 (PECAM-1: ∼552-folds and ANGPT-1: 67-folds) and decreased significantly by Day 21. This downregulation was universal, as by Day 21, no groups in Strategy-1 exhibited highly elevated expression of endotheliogenic markers. Group I, which was formed with a miR-210 transfected ADSCs, displayed a significant upregulation of endotheliogenic markers with Strategy-2 on Day 21. Expression of PECAM-1 for Group III in Strategy-2 on Day 21 (~28-folds) was significantly higher than those in Strategy-1. Our results indicate that assembling a miR-148b transfected spheroid with a miR-210 transfected spheroid (Group III) supported the higher endothelial marker expressions compared to the use of a single miRNA mimic or osteogenic medium.

In order to further confirm the expression of osteogenic markers in doublet structures, RUNX2, an early state osteogenic marker, was determined by immunofluorescent (IF) imaging. At the same time, VE-cadherin staining was performed to confirm the presence of endothelial cells in doublets.

The results for Strategy-1 at Day 7 showed that miR-148b alone resulted in an increased RUNX2 expression, similar to the pattern of RUNX2 expression in Group IV (positive control) (figure 4). Neither Group I (miR-210 alone) nor Group III (the assembly of miR-148b and miR-210 transfected spheroids) had any visible RUNX2 expression. At Day 14, RUNX2 staining was positive for Group II but mainly localized to only one of the spheroids possibly indicating the miR-148b transfected spheroid. At Day 14, there was also observable VE-cadherin expression in Groups I and III, as both contained a miR-210 transfected spheroid while there was no noticeable expression in Groups II and IV, which was the miR-148b alone and positive control group, respectively. IF images also demonstrated that VEcadherin expression for Groups I and III was uniform throughout the entire doublet domain in Strategy-1 at Day 21.

In contrast, Strategy-2 exhibited stronger expression of VE-cadherin for Groups I and III at Day 7 and this expression considerably increased at Day 21 for Group I. Group II showed distinct RUNX2 expression at all time points with a maximal expression at Day 21. Notably, Group III exhibited the strongest fluorescent intensity of RUNX2,

N Celik et al

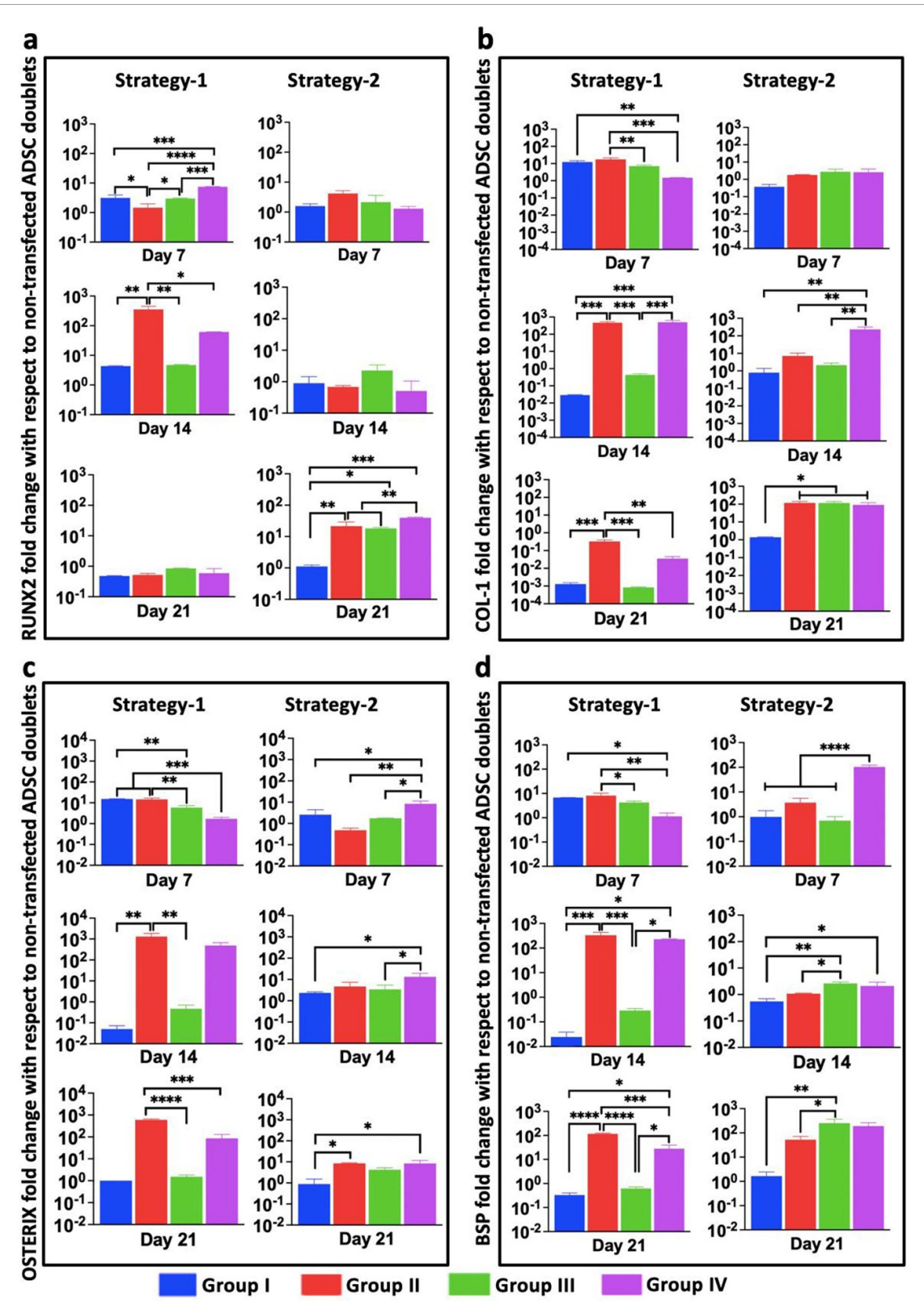


Figure 2. Gene expression levels for Group I (transfected with miR-210), Group II (transfected with miR-148b), Group III (transfected with miR-148b and miR-210), and Group IV (positive control in OM medium) doublets normalized to Group V (negative control in basal medium) doublets for osteogenic markers: (a) RUNX2, (b) Col-1, (c) OSTERIX, and (d) BSP (n = 3; $p^* < 0.05$; $p^{**} < 0.01$; $p^{****} < 0.001$; $p^{****} < 0.001$).

and VE-cadherin compared to other groups in Strategy-2 at Day 21. For Group III, VE-cadherin expression was evident from the early time points while RUNX2 expression was evident from Day 14. Overall, confocal images indicated that Strategy-2 groups had the strongest expression of RUNX2, with maximal expression in Groups II and III at Day 21.

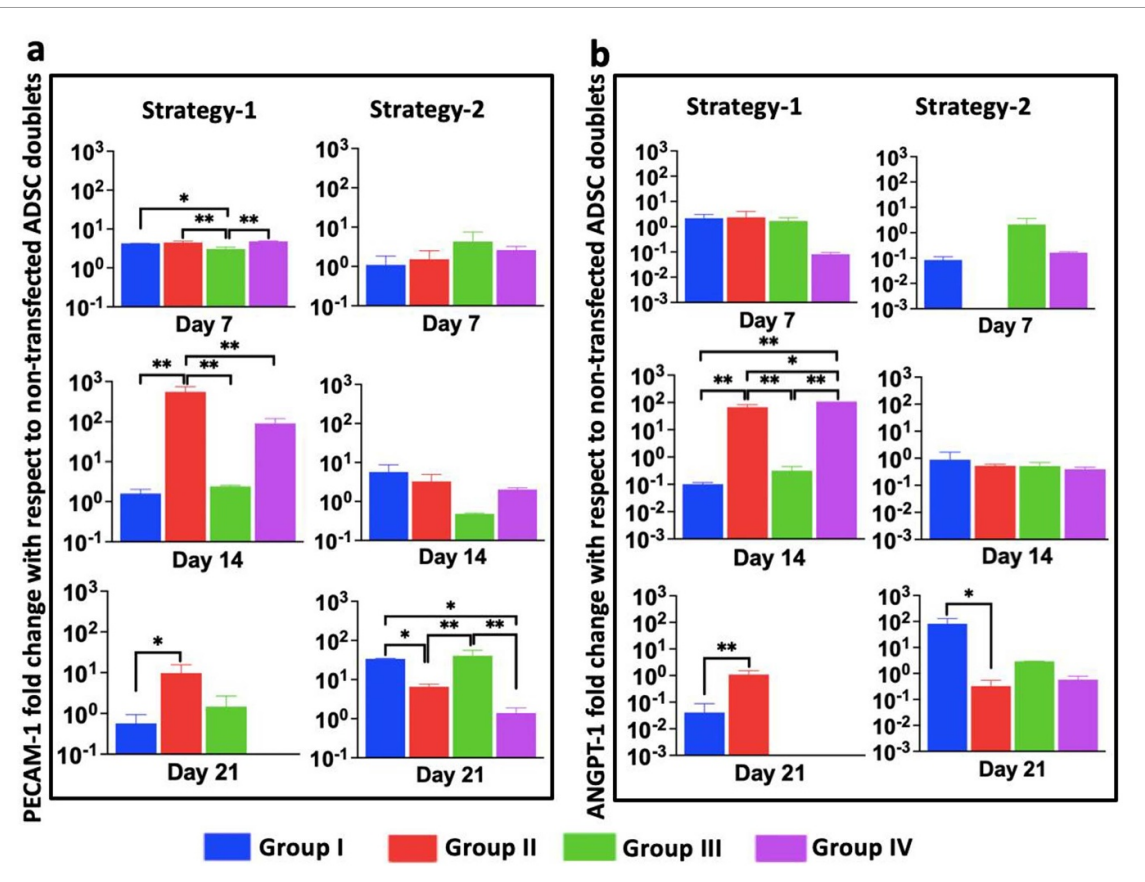


Figure 3. Gene expression levels for Group I (transfected with miR-210), Group II (transfected with miR-148b), Group III (transfected with miR-148b and miR-210), and Group IV (positive control in OM medium) doublets normalized to Group V (negative control in basal medium) doublets for endotheliogenic markers: (a) PECAM-1, and (b) ANGPT-1 (n = 3; $p^* < 0.05$; $p^{**} < 0.01$).

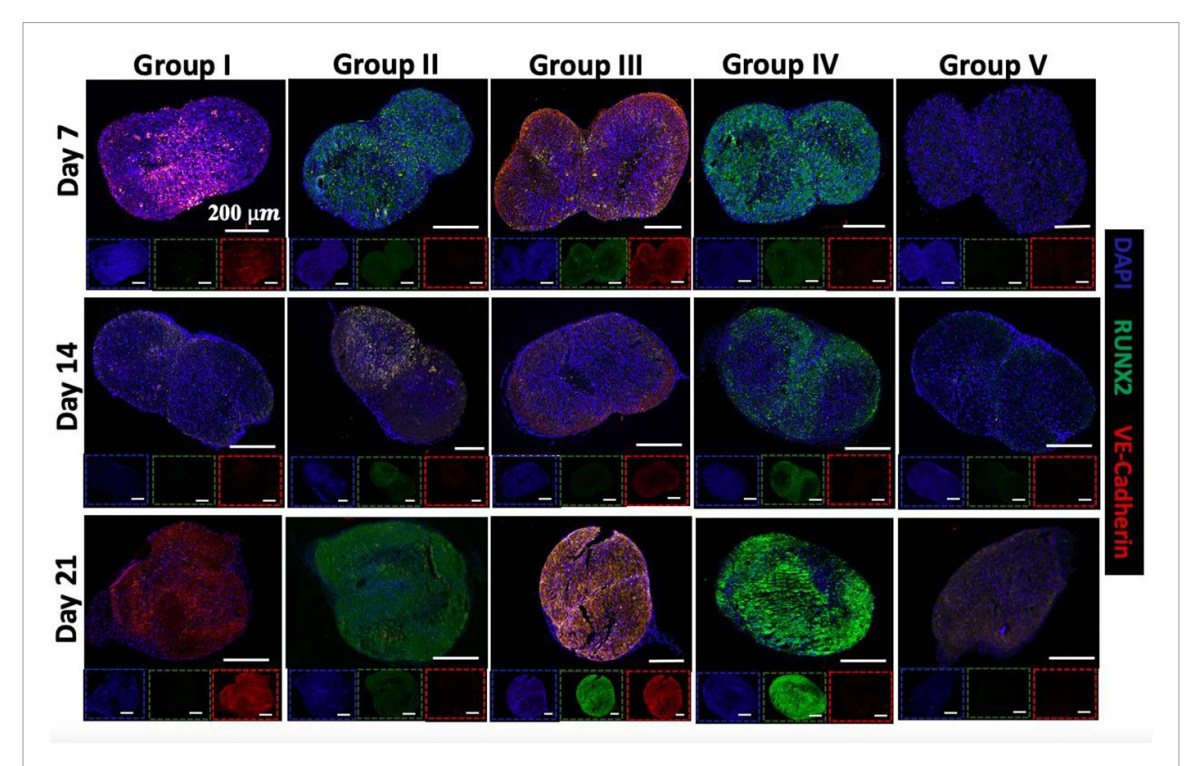


Figure 4. Immunostaining (DAPI in blue, RUNX2 in green, and VE-cadherin in red) images of Strategy-1 (2 d transfection period) doublets of Group I (transfected with miR-210), Group II (transfected with miR-148b), Group III (transfected with miR-148b and miR-210), Group IV (positive control in OM medium), and Group V (negative control in basal medium) at Days 7, 14, and 21. Scale bars in insets correspond to 200 μ m.

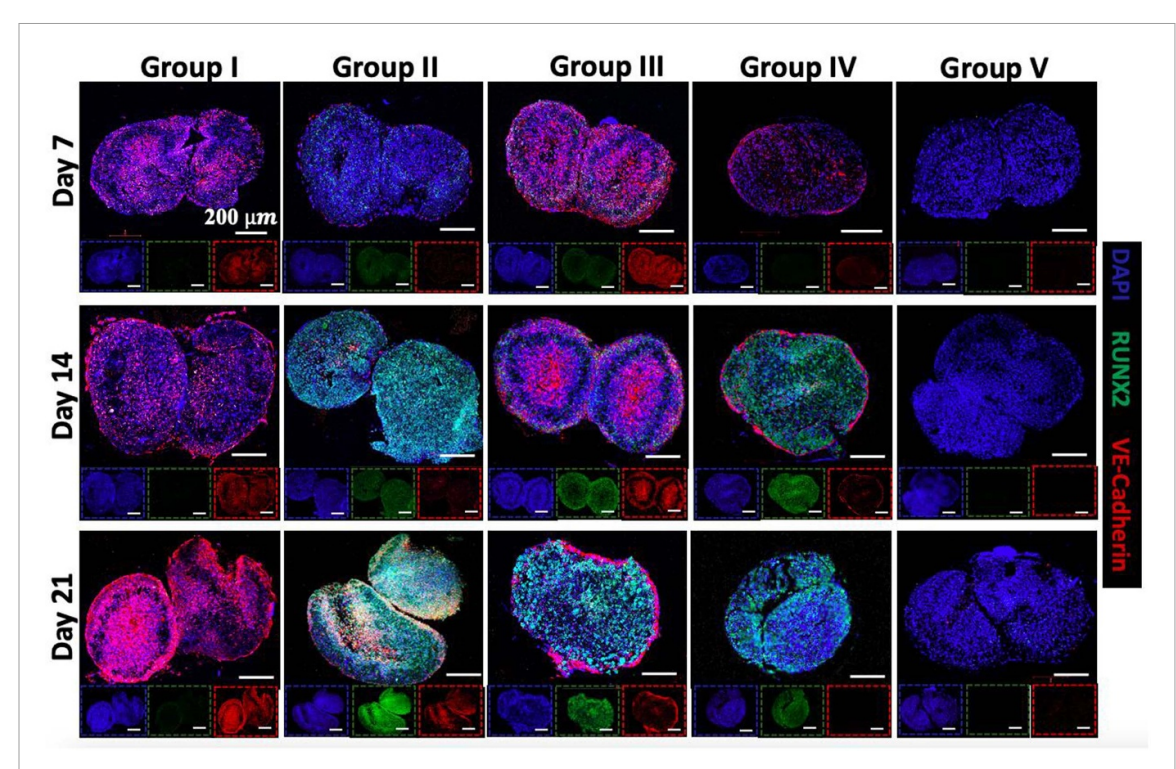


Figure 5. Immunostaining (DAPI in blue, RUNX2 in green, and VE-cadherin in red) images of Strategy-2 (14 d transfection period) spheroids of Group I (transfected with miR-210), Group II (transfected with miR-148b), Group III (transfected with miR-148b and miR-210), Group IV (positive control in OM medium), and Group V (negative control in basal medium) at Days 7, 14, and 21. Scale bars in insets correspond to 200 μ m.

Mineralization was used as an endpoint measure for osteogenic potential of the assembled doublets for all groups and strategies. To determine the extent of mineralization, Osteoimage[™] staining was performed at Days 7, 14, and 21. During mineralization, osteoblasts produce extracellular hydroxyapatite deposits, which is an indication of bone formation [27]. Osteoimage staining showed calcium deposition and specific hydroxyapatite formation in figures 5(a) and (b). In Strategy-1, Groups II and III exhibited significant mineralization, where expression in Group III was similar to that in Group IV (positive control) for all time points. In general, mineralization in Group I was similar in intensity and pattern compared to that in the negative control group. These results indicated that combinations of osteogenic and endotheliogenic committed progenitors with short, 2 d, induction times yielded improved mineralization.

In Strategy-2, substantial mineral deposition was again observed for Group II and III, with an intensity similar to the positive control group at Days 7 and 14 (figure 6(b)). For both groups, the intensity increased overtime, which was significantly greater than that for Group I and the negative control group for all time points. These results indicated that transfection of ADSCs with miR-148b induced bone formation, whether used alone or in conjunction with miR-210 transfected cells. The mean grey scale value (intensity) of osteoimages for Groups II and III in Strategy-2 was ~7.2 and ~7.4 (figure 6(d)), respectively, which was significantly greater than the intensity of same

groups in Strategy-1 (\sim 2.3 and \sim 3.6, respectively) (figure 6(c)).

To determine the morphology and organization of fusing spheroids, H&E staining was conducted for doublets. Images from groups in Strategy-1 demonstrated no obvious difference in staining intensity over 21 d except Group IV doublets, which showed higher density of bone matrix deposition, spheroids in all groups quickly assembled and the doublet structures morphologically evolved into larger spheroids over time (figure 7(a)). Comparatively, H&E images for all groups in Strategy-2 demonstrated more robust staining indicating greater density of the cellular matrix deposition, particularly in Groups II and III, similar to the positive control group (Group IV) (figure 7(b)). In Groups II, III, and IV, doublets showed increasing bone matrix deposition over time. Additionally, most of spheroid pairs maintained a distinct doublet morphology in contrast to those from Strategy-1, where doublet structures turned into a ball shape.

To analyze the fusion of spheroids in doublet structures, morphological changes were imaged at Days 7, 14 and 21 (figures 8(a)–(j)). Doublet length, doublet width, intersphere angle and contact length between spheroids were measured for all groups for both Strategy-1 (figures 8(b)–(e)) and Strategy-2 (figures 8(g)–(j)). In Strategy-1, intersphere angle, doublet width, and contact length increased and doublet length decreased by time. After 14 d of fusion, the intersphere angle reached 180° and did not

N Celik et al

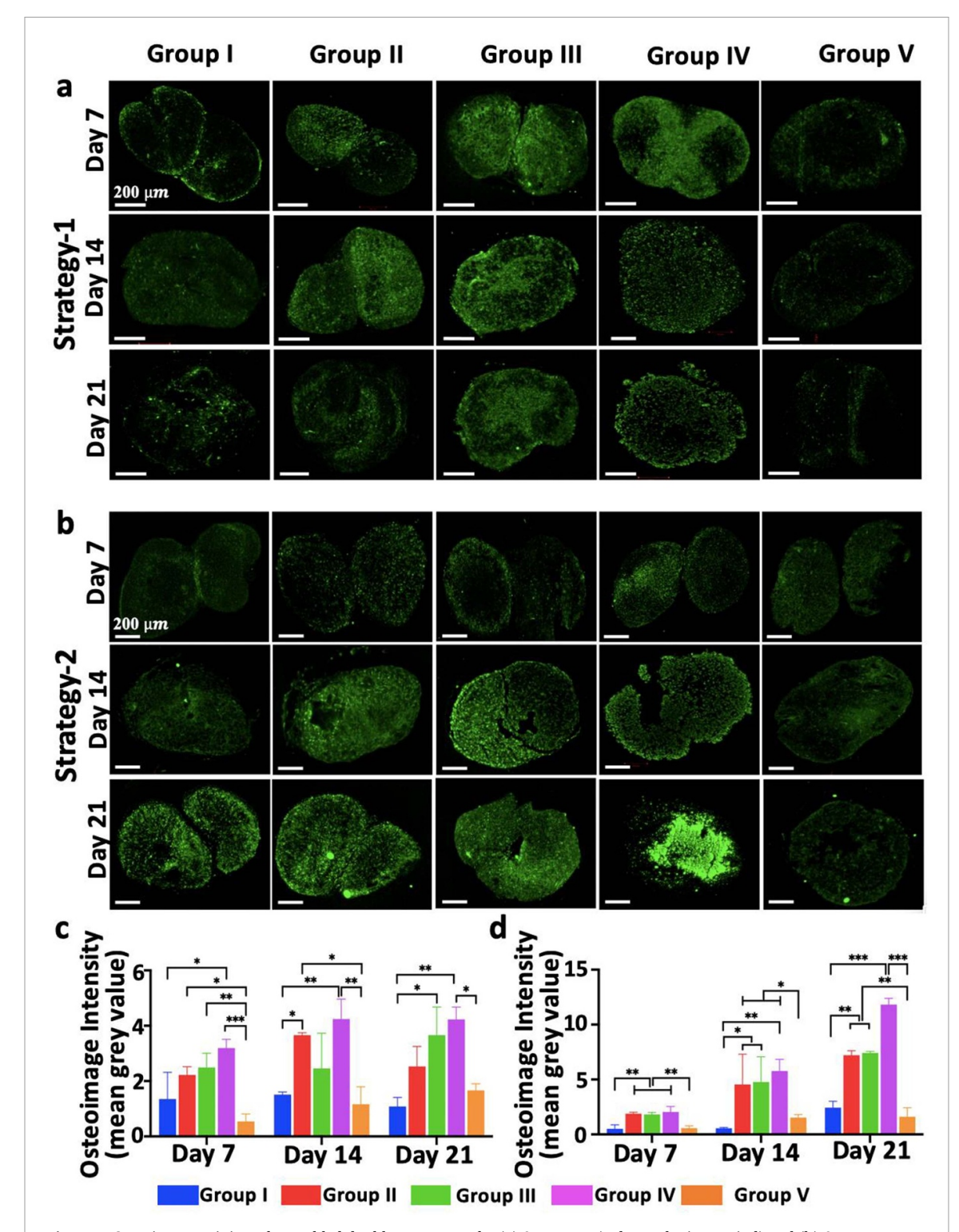


Figure 6. Osteoimage staining of assembled doublet structures for (a) Strategy-1 (2 d transfection period) and (b) Strategy-2 (14 d transfection period). Quantitative intensity analysis of osteoimages for (c) Strategy-1 and (d) Strategy-2 (n=3; $p^*<0.05$; $p^{**}<0.01$; $p^{***}<0.001$). Group I (transfected with miR-210), Group II (transfected with miR-148b), Group III (transfected with miR-148b and miR-210), Group IV (positive control in OM medium), and Group V (negative control in basal medium) at Days 7, 14, and 21.

change any further. The contact length approached the width of spheroids indicating complete fusion. In Strategy-1, fused spheroids after 21 d of culture displayed a more rounded morphology compared to the oval-shape spheroids at Day 14 (figure 8(a)). In Strategy-2, doublet width and contact length increased until Day 14 and showed a stable trend

afterwards. Doublet length showed a small decrease by time. After 21 d of fusion, the intersphere angle did not change significantly. In Strategy-2, doublet structures maintained their morphology.

In this work, a custom-made bioprinter was used to fabricate a simplistic model of the Haversian canal as a proof of concept study. To visualize

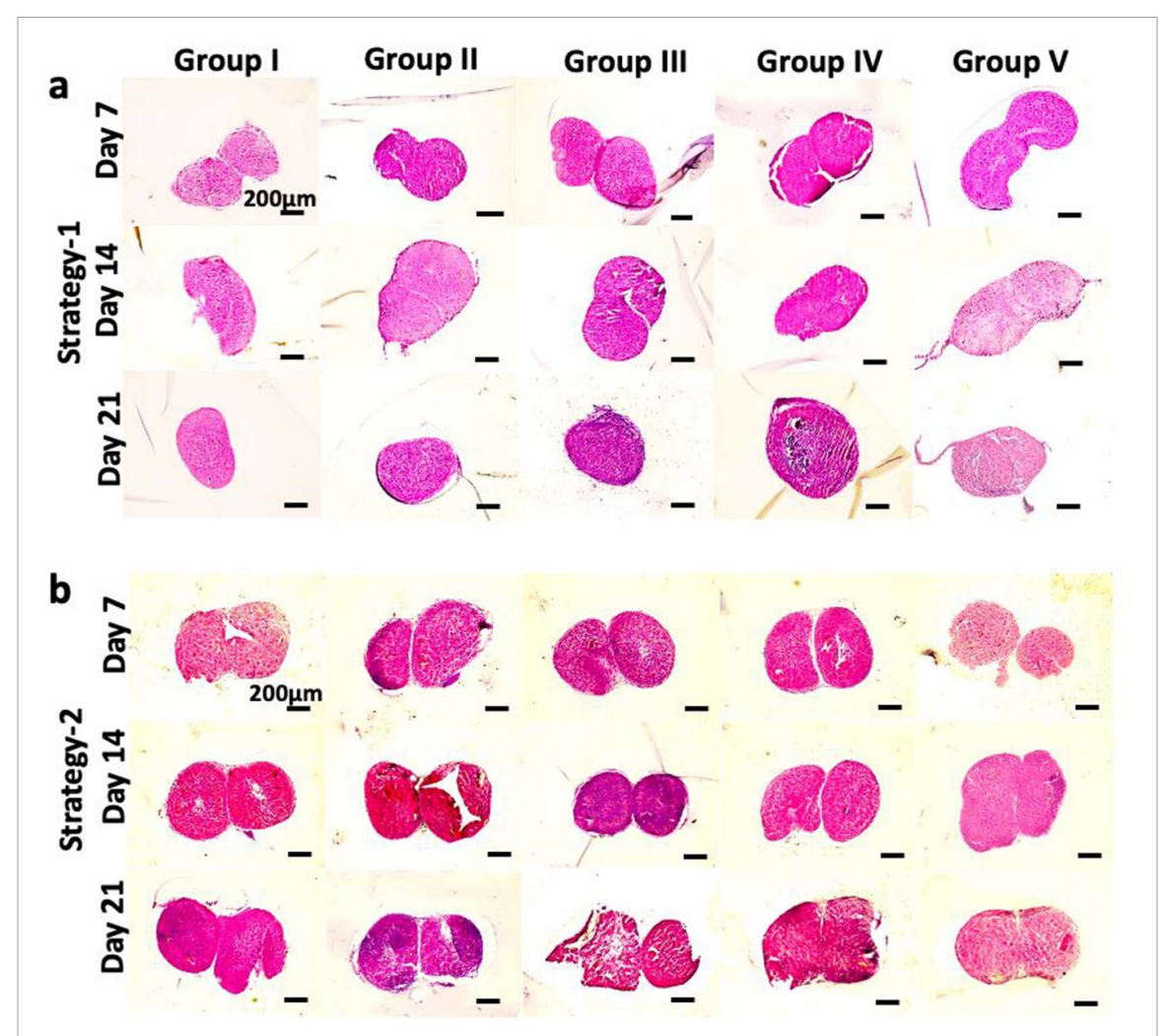


Figure 7. H&E images of doublet structures of (a) Strategy-1 (2 d transfection period) and (b) Strategy-2 (14 d transfection period) for Group I (transfected with miR-210), Group II (transfected with miR-148b), Group III (transfected with miR-148b and miR-210), Group IV (positive control in OM medium), and Group V (negative control in basal medium) at Days 7, 14, and 21.

the bioprinting process and positioning of spheroids in the fabricated hollow structures, ADSCs spheroids labelled with CellTracker™ green CMFDA dye and CellTracker™ Red CMTPX dye were bioprinted sequentially (figures 9(a) and (b), supplementary video 1). Both circular and square shape hollow structures were bioprinted into the support bath consisting of alginate microgels to demonstrate the versatility of the approach. In order to pattern osteogenic and endotheliogenic spheroids, Group III spheroids transfected with miR-148b and miR-210 were utilized for bioprinting, respectively. First, miR-210-transfected spheroids were bioprinted in a ring form and then miR-148b-transfected spheroids were bioprinted to encircle the miR-210transfected ones. Fourteen days post bioprinting, spheroids were assembled through fusion and IHC and H&E staining was performed to demonstrate the tissue morphology and histology. Both sides were distinguishable throughout the intensity of IHC images, where osteogenic outer zone (transfected with miR-148b) showed increased RUNX2

intensity and endotheliogenic inner zone (transfected with miR-210) showed distinguishable VE Cadherin intensity (figures 9(c) and (d)). H&E staining showed bone matrix deposition around the periphery of the bioprinted structure, where most of the spheroids were fused (figure 9(e)); however, disassembly of some spheroids was also observed in the bioprinted structure due to the limited fusion of these spheroids.

4. Discussions

Vascularization is essential to supply cells with nutrients and prevent hypoxia-induced cell death after implantation of engineered tissue constructs. Although, ADSCs secrete potent growth factors, such as fibroblast growth factor-2 and vascular endothelial growth factor (VEGF), it is often not adequate to stimulate angiogenesis which has a vital importance to support nutrient supply and tissue integration as well as osteogenesis [28–31]. To enhance vascularization, many studies utilized a co-culture system with a terminally differentiated cell type, such as

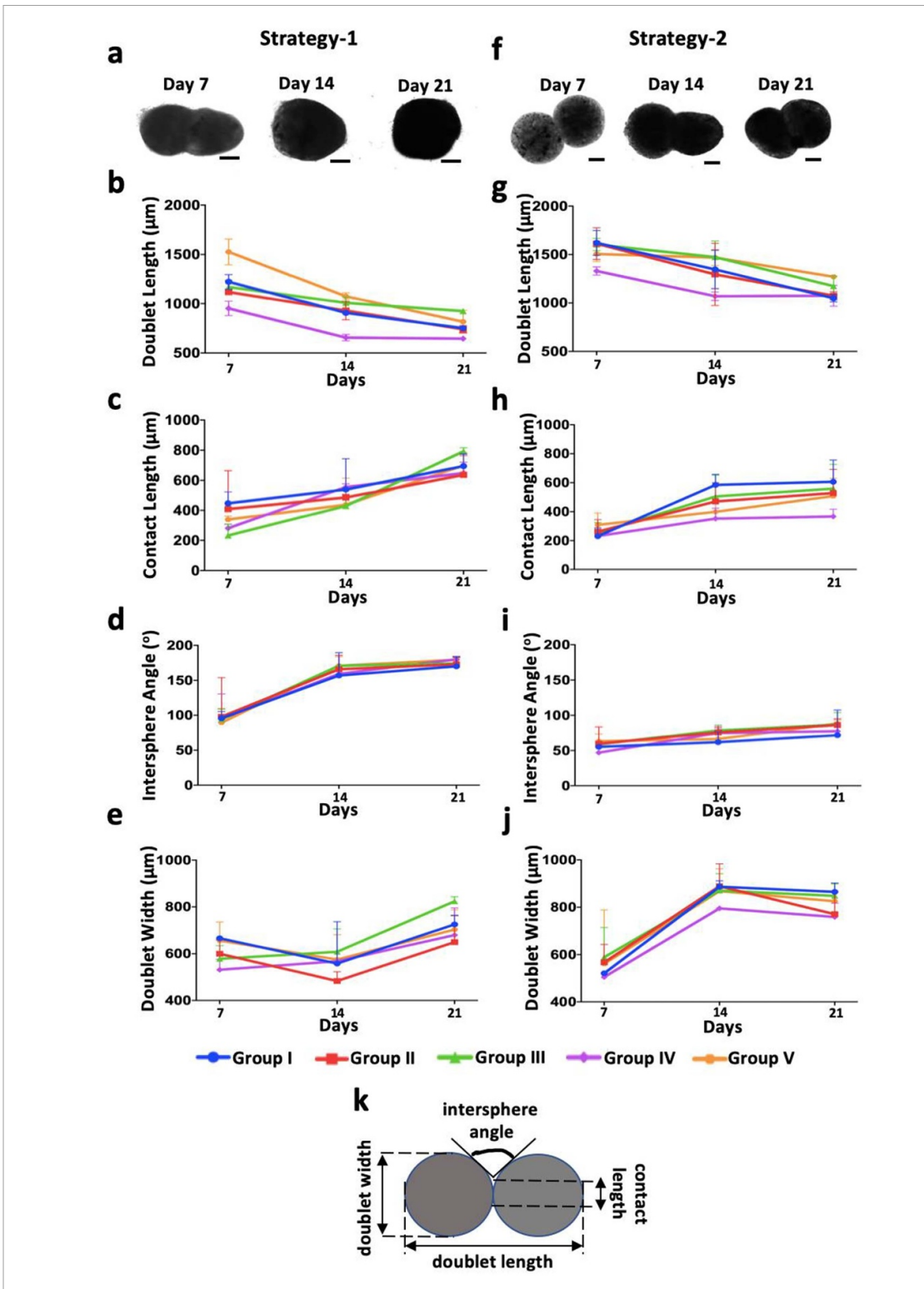


Figure 8. Characterization of spheroid fusion in doublets. For Strategy-1 (2 d transfection period), (a) representative light microscopy images of fusing spheroids in assembled doublet structures over the 21 d timeframe and corresponding parameters including (b) doublet length (μ m), (c) contact length (μ m), (d) intersphere angle (°), and (e) doublet width (μ m). For Strategy-2 (14 d transfection period), (f) representative light microscopy images of fusing spheroids in assembled doublet structures over the 21 d timeframe and corresponding parameters including (g) doublet length (μ m), (h) contact length (μ m), (i) intersphere angle (°), and (j) doublet width (μ m). (k) A schematic showing morphological parameters measured during fusion.

human umbilical vein endothelial cells (HUVECs) [31]. However, using of mature (primary) cells, such as HUVECs, often results in low proliferation and division potential as these are post-mitotic cells [32]. In addition, using mature cells often results in loss

of tissue volume and disorganized tissue interfaces. Moreover, such cells have limited clinical translation potential. The use of stem/progenitor cells to recapitulate heterotypic vascularized tissue is complicated by a poorly understood process of co-differentiation

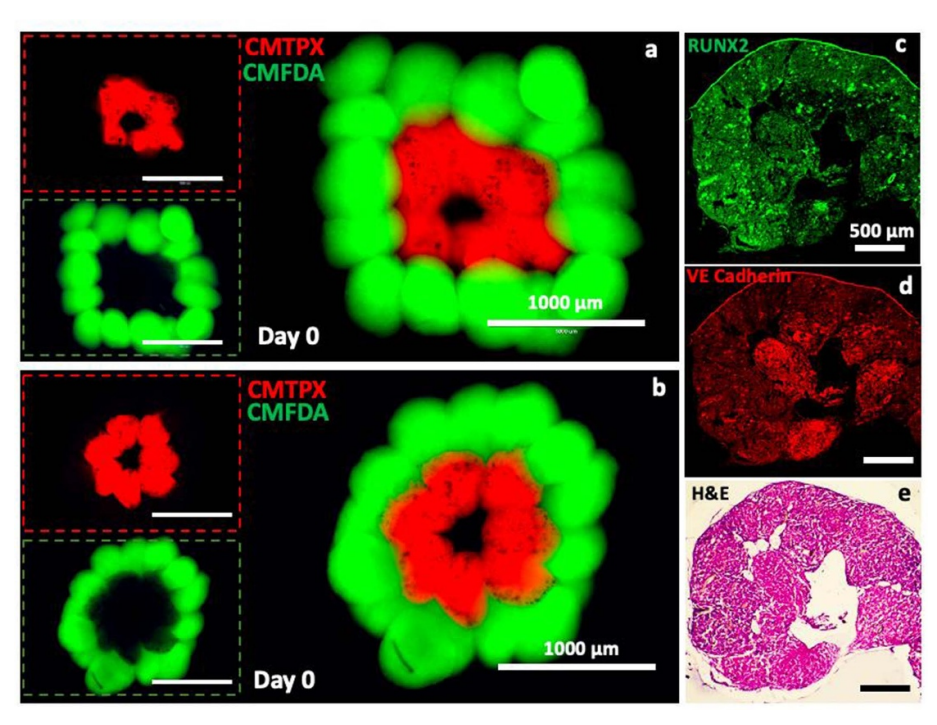


Figure 9. Representation and characterization of the Haversian canal model fabricated using the aspiration-assisted bioprinting technique. (a), (b) Bioprinted structures consisted of ADSCs spheroids labeled with CellTrackerTM green CMFDA dye and CellTrackerTM Red CMTPX dye post bioprinting. Immunoimages, showing (c) RUNX2 and (d) VE-cadherin, and (e) a H&E image of a bioprinted structure at Day 14 post bioprinting.

where environmental cues and cellular heterogeneity (genetic, epigenetic, cell signaling) complicate the prediction of cell differentiation in heterotypic systems [33]. While there are established 2D culture techniques to drive differentiation of ADSCs into osteogenic, endotheliogenic, adipogenic and chondrogenic lineages [34], these processes result in largely uniform populations, not the heterotypic populations that are required to mimic or repair complex functional tissues, such as bone, muscle, adipose or cartilage.

It is clear that there is crosstalk during heterotypic differentiation, such as the reciprocal relationship between adipogenic and endotheliogenic fates mediated by VEGF [35, 36] or adipogenic and osteogenic fate mediated by peroxisome proliferator-activated receptor gamma (PPAR- γ) [37]. VEGF has also been shown to be a key paracrine regulator of endotheliogenesis and osteogenesis during bone repair [38]. In addition, previous studies have described the upregulation of angiogenic markers including ANGPT1, LEP and HGF as well as the proangiogenic chemokines CXCL1, CXCL5, CXCL6, and CXCL8 during osteogenesis of ADSCs. Osteogenesis promotes endothelial differentiation in early stages of endotheliogenesis [39]. During development, synchronization of chondrogenic, osteogenic and endotheliogenic differentiation processes occurring in adjacent tissues is regulated through vigorous crosstalk between the cell types [40]. Efforts to understand these complex processes in native tissues use reverse engineering to

identify the differentiation cues that guide progenitor cells to distinct cell fates [41]. Despite being an active area of research, directing homotypic progenitor co-differentiation into heterotypic organoids and tissues remains poorly understood.

Using miRNA to modulate the differentiation of progenitors in spheroids has the potential to overcome the limitations associated with mature vascular cells to improve the survival and integration of large complex tissue grafts. A previous study has shown that miR-210 is a potential factor for stimulating focal angiogenesis and its over expression can promote vascular endothelial cell proliferation [42]. Here, we also revealed that miR-210 could promote vascular endothelial cell differentiation as both shortand long-term differentiation in 3D engineered tissue structures. In agreement with previously published results on miR-148b overexpression, all the assayed osteogenic genes were significantly upregulated in groups transfected with miR-148b (Groups II and III) for both Strategy-1 and Strategy-2 (figure 2). Gene analysis, immunostaining and osteoimage results showed improved differentiation and mineralization for both Strategy-1 and Strategy-2 in Group II and Group III. Importantly, when induced for 14 d (Strategy-2), the combination of spheroids transfected with miR148b and miR210 mimics in Group III resulted in upregulation of both endotheliogenic and osteogenic markers expression.

Also, the results showed that doublet structures assembled from spheroids cultured longer in 2D

after miRNA transfection (Strategy-2) maintained their original shape (doublet) as evidenced by the staining results (figures 4–7) and size measurements (figure 8). This could be due to the fact that longer incubation in 2D promoted better differentiation of committed progenitors, which in turn reduced their proliferation resulting in slower and limited fusion of spheroids after their assembly. This potentially addresses another concern of complex 3D graft fabrication, as compaction-related shape change is a challenge in fabrication of organized, large scale tissue grafts [24].

While both Strategy-1 and Strategy-2 showed upregulated osteogenic and endotheliogenic gene and protein expressions, Strategy-2 demonstrated significantly greater expression of the evaluated markers in all experiments. Group III results, formed using a miR-210 and a miR-148b transfected spheroid, revealed that simultaneous co-differentiation supported both differentiation paths when we compared with the individually transfected groups (Groups I and II).

The bioprinted tissue presented in figure 9 demonstrates a simplistic model of the Haversian canal, where miR-210-transfected endotheliogenic spheroids were arranged into a ring form, which were encircled by miR-148b-transfected osteogenic spheroids. For future work, both arteries and veins as well as nerves and lymphatic vessels should be reconstituted in 3D to better mimic the Haversian canal. In this regard, smaller spheroids should be used to increase the resolution of the bioprinting process to better recapitulate the above-mentioned components of the Haversian canal. After bioprinting, we also observed limited fusion of some spheroids, which could be due to support bath related issues, such as the presence of larger alginate microgels between spheroids restricting the self-assembly of spheroids, as elaborated in our recent work [24]. Therefore, the support bath should be further engineered in order to enhance the fusion capacity of spheroids for scalable tissue fabrication.

5. Conclusions

In this research, we have successfully fabricated doublet structures using spheroids of ADSCs transfected by miR-148b, and miR-210, and evaluated their osteogenic and endothelial differentiation, mineralization, and bone formation potential. Our results showed that the transfection of ADSC spheroids as doublet structures (a) induced endothelial differentiation of ADSCs by transfection with miR-210 mimic, (b) improved osteogenic differentiation using miR-148b transfection, (c) improved compaction-related shape changes, and (d) drove co-differentiation of stem cells allowing the formation of complex heterotypic structures. Therefore, our findings suggest that spheroids, made of ADSCs cultured long-term in 2D

post transfection, can be a useful strategy for vascularized bone tissue fabrication. In the future, we plan to further investigate 3D bioprinting in order to generate large scale bone tissues.

Data availability statement

All data that support the findings of this study are included within the article (and any supplementary files).

Acknowledgments

This work was supported by the National Institute of Dental and Craniofacial Research of the National Institutes of Health under Award Number RDE024790A (D J H), R01DE028614 (I T O), and the National Science Foundation award number 2033673 (D J H) and 1914885 (I T O). The authors thank R&D Systems (Minneapolis, MN) for providing several reagents. We also thank Dr S Koduru and Dr D from Penn State Department of Surgery for providing ADSCs in support of our experiments and Dr A Salem from University of Iowa for fruitful discussions. N C acknowledges the support from the Turkish Ministry of National Education. The opinions, interpretations, conclusions, and recommendations are those of the author and are not necessarily endorsed by National Institutes of Health or National Science Foundation.

Conflict of interest

The authors declare no competing interests.

ORCID iD

Ibrahim T Ozbolat https://orcid.org/0000-0001-8328-4528

References

- [1] Soucacos P N, Kokkalis Z T, Piagkou M and Johnson E O 2013 Vascularized bone grafts for the management of skeletal defects in orthopaedic trauma and reconstructive surgery *Injury* 44 S70–5
- [2] Amini A R, Laurencin C T and Nukavarapu S P 2012 Bone tissue engineering: recent advances and challenges Crit. Rev. Biomed. Eng. 40 363–408
- [3] Cai X, Yang F, Yan X, Yang W, Yu N, Oortgiesen D A W, Wang Y, Jansen J A and Walboomers X F 2015 Influence of bone marrow-derived mesenchymal stem cells pre-implantation differentiation approach on periodontal regeneration in vivo J. Clin. Periodontol. 42 380–9
- [4] Kuhn L T et al 2014 Developmental-like bone regeneration by human embryonic stem cell-derived mesenchymal cells Tissue Eng. A 20 365–77
- [5] Eppler S M, Combs D L, Henry T D, Lopez J J, Ellis S G, Yi J-H, Annex B H, McCluskey E R and Zioncheck T F 2002 A target-mediated model to describe the pharmacokinetics and hemodynamic effects of recombinant human vascular endothelial growth factor in humans Clin. Pharmacol. Ther. 72 20–32
- [6] Moncal K K, Aydin R S T, Abu-Laban M, Heo D N, Rizk E, Tucker S M, Lewis G S, Hayes D and Ozbolat I T 2019

- Collagen-infilled 3D printed scaffolds loaded with miR-148b-transfected bone marrow stem cells improve calvarial bone regeneration in rats *Mater. Sci. Eng.* C **105** 110128
- [7] Grottkau B E and Lin Y 2013 Osteogenesis of adipose-derived stem cells *Bone Res.* 1 133–45
- [8] Dai R, Wang Z, Samanipour R, Koo K-I and Kim K 2016 Adipose-derived stem cells for tissue engineering and regenerative medicine applications *Stem. Cells Int.* 2016 1–19
- [9] Song L and Tuan R S 2006 MicroRNAs and cell differentiation in mammalian development *Birth Defects Res.* C 78 140–9
- [10] Clancy J L et al 2014 Small RNA changes en route to distinct cellular states of induced pluripotency Nat. Commun. 5 1–9
- [11] Qureshi A T, Doyle A, Chen C, Coulon D, Dasa V, del Piero F, Levi B, Monroe W T, Gimble J M and Hayes D J 2015 Photoactivated miR-148b—nanoparticle conjugates improve closure of critical size mouse calvarial defects *Acta Biomater.* 12 166–73
- [12] Lian J B, Stein G S, van Wijnen A J, Stein J L, Hassan M Q, Gaur T and Zhang Y 2012 MicroRNA control of bone formation and homeostasis Nat. Rev. Endocrinol. 8 212
- [13] Liao Y-H, Chang Y-H, Sung L-Y, Li K-C, Yeh C-L, Yen T-C, Hwang S-M, Lin K-J and Hu Y-C 2014 Osteogenic differentiation of adipose-derived stem cells and calvarial defect repair using baculovirus-mediated co-expression of BMP-2 and miR-148b *Biomaterials* 35 4901–10
- [14] Qureshi A T, Monroe W T, Dasa V, Gimble J M and Hayes D J 2013 miR-148b—nanoparticle conjugates for light mediated osteogenesis of human adipose stromal/stem cells Biomaterials 34 7799–810
- [15] Chan Y C, Banerjee J, Choi S Y and Sen C K 2012 miR-210: the master hypoxamir *Microcirculation* 19 215–23
- [16] Hutmacher D W 2001 Scaffold design and fabrication technologies for engineering tissues—state of the art and future perspectives J. Biomater. Sci. Polym. Ed. 12 107–24
- [17] Mironov V, Visconti R P, Kasyanov V, Forgacs G, Drake C J and Markwald R R 2009 Organ printing: tissue spheroids as building blocks *Biomaterials* 30 2164–74
- [18] Langer R 2007 Tissue engineering: perspectives, challenges, and future directions *Tissue Eng.* 13 1–2
- [19] Engler A J, Sen S, Sweeney H L and Discher D E 2006 Matrix elasticity directs stem cell lineage specification *Cell* 126 677–89
- [20] Laschke M W and Menger M D 2017 Life is 3D: boosting spheroid function for tissue engineering *Trends Biotechnol*. 35 133–44
- [21] Wu Y, Hospodiuk M, Peng W, Gudapati H, Neuberger T, Koduru S, Ravnic D J and Ozbolat I T 2018 Porous tissue strands: avascular building blocks for scalable tissue fabrication *Biofabrication* 11 015009
- [22] Wu Y, Ayan B, Moncal K K, Kang Y, Dhawan A, Koduru S V, Ravnic D J, Kamal F and Ozbolat I T 2020 Hybrid bioprinting of zonally stratified human articular cartilage using scaffold-free tissue strands as building blocks Adv. Healthcare Mater. 9 2001657
- [23] de Moor L, Fernandez S, Vercruysse C, Tytgat L, Asadian M, de Geyter N, van Vlierberghe S, Dubruel P and Declercq H 2020 Hybrid bioprinting of chondrogenically induced human mesenchymal stem cell spheroids Front. Bioeng. Biotechnol. 8 484
- [24] Ayan B, Celik N, Zhang Z, Zhou K, Kim M H, Banerjee D, Wu Y, Costanzo F and Ozbolat I T 2020 Aspiration-assisted freeform bioprinting of pre-fabricated tissue spheroids in a yield-stress gel Commun. Phys. 3 1–14
- [25] Kim M H, Banerjee D, Celik N and Ozbolat I T 2021 Aspiration-assisted freeform bioprinting of mesenchymal

- stem cell spheroids within alginate microgels *bioRxiv* (https://doi.org/10.1101/2021.07.13.452209)
- [26] Ayan B, Heo D N, Zhang Z, Dey M, Povilianskas A, Drapaca C and Ozbolat I T 2020 Aspiration-assisted bioprinting for precise positioning of biologics Sci. Adv. 6 eaaw5111
- [27] Jaiswal N, Haynesworth S E, Caplan A I and Bruder S P 1997 Osteogenic differentiation of purified, culture-expanded human mesenchymal stem cells in vitro J. Cell. Biochem. 64 295–312
- [28] Böhrnsen F and Schliephake H 2016 Supportive angiogenic and osteogenic differentiation of mesenchymal stromal cells and endothelial cells in monolayer and co-cultures *Int. J. Oral. Sci.* 8 223–30
- [29] Pekozer G G, Kose G T and Hasirci V 2016 Influence of co-culture on osteogenesis and angiogenesis of bone marrow mesenchymal stem cells and aortic endothelial cells *Microvasc. Res.* 108 1–9
- [30] Li Q and Wang Z 2013 Influence of mesenchymal stem cells with endothelial progenitor cells in co-culture on osteogenesis and angiogenesis: an in vitro study Arch. Med. Res. 44 504–13
- [31] Heo D N, Hospodiuk M and Ozbolat I T 2019 Synergistic interplay between human MSCs and HUVECs in 3D spheroids laden in collagen/fibrin hydrogels for bone tissue engineering Acta Biomater. 95 348–56
- [32] Buttery L D and Bishop A E 2005 Introduction to tissue engineering *Biomaterials*, *Artificial Organs and Tissue Engineering* (United Kingdom: Woodhead Publishing) pp 193–200
- [33] Shakiba N et al 2019 Cell competition during reprogramming gives rise to dominant clones Science 364 eaan0925
- [34] Gimble J M, Katz A J and Bunnell B A 2007 Adipose-derived stem cells for regenerative medicine Circ. Res. 100 1249–60
- [35] Fukumura D, Ushiyama A, Duda D G, Xu L, Tam J, Krishna V, Chatterjee R K, Garkavtsev I and Jain R K 2003 Paracrine regulation of angiogenesis and adipocyte differentiation during in vivo adipogenesis Circ. Res. 93 e88–97
- [36] Hammel J H and Bellas E 2020 Endothelial cell crosstalk improves browning but hinders white adipocyte maturation in 3D engineered adipose tissue *Integr. Biol.* 12 81–9
- [37] Zhuang H, Zhang X, Zhu C, Tang X, Yu F, Shang G W and Cai X 2016 Molecular mechanisms of PPAR-γ governing MSC osteogenic and adipogenic differentiation *Curr. Stem. Cell Res. Ther.* 11 255–64
- [38] Genova T, Petrillo S, Zicola E, Roato I, Ferracini R, Tolosano E, Altruda F, Carossa S, Mussano F and Munaron L 2019 The crosstalk between osteodifferentiating stem cells and endothelial cells promotes angiogenesis and bone formation Front. Physiol. 10 1291
- [39] Shaik S, Martin E C, Hayes D J, Gimble J M and Devireddy R V 2019 Transcriptomic profiling of adipose derived stem cells undergoing osteogenesis by RNA-Seq Sci. Rep. 9 1–17
- [40] Maes C 2017 Signaling pathways effecting crosstalk between cartilage and adjacent tissues: seminars in cell and developmental biology: the biology and pathology of cartilage Seminars in Cell & Developmental Biology vol 62 (New York: Academic) pp 16–33
- [41] Tewary M, Shakiba N and Zandstra P W 2018 Stem cell bioengineering: building from stem cell biology *Nat. Rev. Genet.* 19 595–614
- [42] Zeng L, He X, Wang Y, Tang Y, Zheng C, Cai H, Liu G Y, Wang Y, Fu Y and Yang G-Y 2014 MicroRNA-210 overexpression induces angiogenesis and neurogenesis in the normal adult mouse brain *Gene Ther.* 21 37–43